Pergamon

Vacuum/volume 51/number 3/pages 339 to 343/1998

0042–207X/98 $19.00+.00

PII : S0042–207X(98)00110–9

Experimental investigation of weld pool formation in electron beam welding

Peter Petrov,[a]* Chavdar Georgiev[a] and Georgy Petrov[b] [a]*Institute of Electronics, 72 Tzarigradsko Chausse, 1784 Sofia, Bulgaria ;* [b]*Institute of Astrophysics, 72 Tzarigradsko Chausse, 1784 Sofia, Bulgaria*

received 6 January 1998

The energy transfer mechanism from an electron beam to a metal target, weld pool and keyhole of formation during electron beam welding was studied using a collector for secondary emitted particles, light photo diodes and CCD techniques. The physical processes in the welding pool and plasma cavity are discussed. It is shown that the nature of the heat source in a weld pool is non-stationary and the dynamic processes occurring in both the welding pool and the plasma cavity play a dominant role in the formation of the welding seam during electron beam welding of metals. Periodical molten metal flows were determined at low oscillation frequencies of the welding seam's root for frequency between 0.5 and 50 Hz and on the surface of the welding pool in the interval 5–850 Hz. The frequency spectrum of the secondary electron emission signal is in the order of a few kHz. © 1998 Elsevier Science Ltd. All rights reserved

1. Introduction

Electron beam welding of materials has a number of decisive advantages over conventional techniques. The focused electron beam is one of the highest power density sources and thus high processing speeds are possible and narrow welds with a narrow heat affected zone can be produced accurately. An important problem in the electron beam welding is the control over the quality of the welding seam.[1] The formation of pores, deformations and tenses during the process of welding lowers significantly the quality of the welded materials. Depending on the power density distribution of the electron beam, welding speed and materials properties, a number of different physical processes such as heat conduction, phase transition, fluid dynamics, evaporation kinetics, and plasma dynamics are involved determining the processing results. When welding with an electron beam at high intensities a focused beam leads to molten material being evaporated with a capillary in the melt (plasma cavity) also formed ; in literature the capillary is called a keyhole.[2] The greatest problem from the practice point of view is provided by the keyhole because in the electron beam radiation is absorbed efficiently. Keyhole formation during electron beam welding has been observed experimentally using X-ray probing[3–6] with high-speed photo-camera,[7,8] photodiodes[9] and various secondary emitted beams such as thermal electrons, metal ions backscattered and secondary electron emission.[10–12] It was found that both the shape and dimensions of a keyhole vary with time, whereby the cavity is periodically filled with liquid metal. These instabilities could be responsible for typical electron beam welding defects such as spiking or ripple formation and it is shown that the instabilities of the keyhole is a result of interaction between metal vapours, electron beam and the cavity walls. The frequency of the filling is of the order of a few Hz and is observed on the weld surface as a cooled ripple weld surface and spiking in the weld root.

This paper describes experimental investigations in monitoring the welding pool and keyhole behaviour during electron beam welding using a charged coupled device (CCD) camera, secondary emitted beams and photodiodes.

2. Experimental method

The experimental arrangement used in the present work is shown on Fig. 1. An electron beam 1 formed in an electron optical system interacts with a moving metal target 3 and a welding seam is created. The CCD camera 4 is used for observation of the molten pool, keyhole, metal vapour and plasma above the surface of the welded specimen. In other works[13,14] it has been shown that in the weld pool boundary the distribution of the average brightness level is 1.5 times more than the one-degree lower level. That way, the pool borderline can be determined by means of calculating the number of pixels of each brightness level from the lower to higher. This method we used in our investigations. The main equipment used to registrar the liquid metal and keyhole picture was a Santa Barbara Instrument Group's CCD camera model ST-8. The active region of the CCD is KAF1600 chip with 13.8×9.2 mm^2 and 1530×1020 pixels 9×9 μm each. The original

* Corresponding author. Fax : 00359 2 97 53201. E-mail : pitiv@phys.acad.bg.

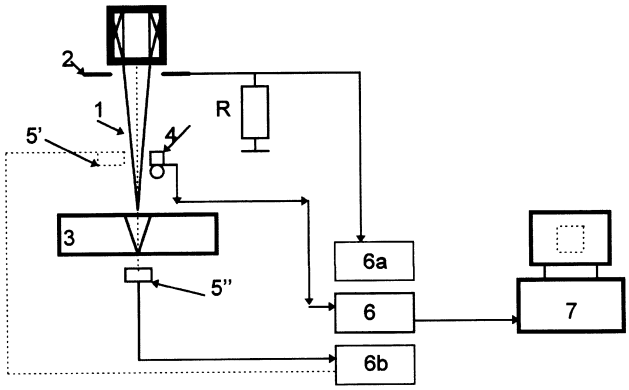

Figure 1. Experimental arrangement.

software of the CCD camera allows rebinding of the image, so the original pictures taken during the experiment were 765×510 pixels each. The exposure times were 10 s, so a neutral wedge was used to lower the illumination. The CCD was cooled to 10°C by a thermoelectric cooler. Standard procedures were used to subtract the dark current, and reduction of the images was taken by ESO_MIDAS 95NOV software package (European South Observatory).

Secondary emitted beams from the welded specimens were detected using a disk collector 2. The analogue signal obtained was amplified and transformed in an analogue–digital convector 6a and processed by a personal computer 7. The collector was made from two electrical connected copper semicircles. This was placed 30 cm above the sample and isolated from the electron beam vacuum chamber. The collector construction was suitable for measurement of the secondary particle flow that includes all types of charged particles characteristic of the electron beam welding processes–ions : thermal, secondary emitted and reflected electrons. The different parts of the secondary emitted flow were investigated by applying positive or negative (appropriate) electrical potential to the collector. The signal of the negative charged collector was formed by the positive ion flow and by the reflected fast electron flow. When the collector potential was positive, the signal results chiefly from the backscattered electrons.

For estimating light emission the detector 5 was placed above the surface 5′ and under the reverse side 5″ of the moveable metal and connected with a PC system 7 through a controller 6b. The light estimator consists of the systems for positioning and projecting the spot to be measured, and a light-frequency converter. The light frequency converter is a silicon photodiode with a current-to-frequency converter on a single monolithic CMOS integrated circuit. A function of the light-frequency convector block diagram is shown in Fig. 2. The output is a square wave (50% duty cycle) with frequency directly proportional to light intensity with a sensitivity of the photodiode between 300 nm and 1100 nm. The obtained data in the PC is stored automatically in a text file which is processed through a specially designed software program including the transition from the static characteristic of the light-to-frequency converter—$T(^\circ\mathrm{C}) = f(F)$ to the measured in real time temperature. The static characteristics $T(^\circ\mathrm{C}) = f(F)$ is formed beforehand. This is because the frequency obtained by the current-frequency converter depends on the type of material from which the radiating surface is made, the distance between the converter and the radiation surface, the spot's diameter etc. The method formation of the numerator's static characteristic $T(^\circ\mathrm{C}) = f(F)$ is described in detailed.[9]

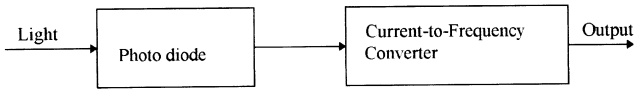

Figure 2. Functional block diagram of the light-to-frequency converter.

All experiments were made using Leybold Heraeus 300/15-60 equipment, with specimens made from carbon steel. The electron beam technological parameters were: acceleration voltage $U = 60$ kV, beam current $I = 20$–250 mA, welding speed $V = 0.5$–5 mm/s, current of focused lens $l_f = 512$ mA.

3. Results and analysis

Figure 3(a) shows typical temporal behaviour of the registered collector signal at a collector potential of +20 V. The Fourier spectrum is represented in the Fig. 3(b). These results show the nonstationary character of the reflected electron signal during the continued mode of beam target interaction. The signal directly depends on the processes in the welding pool and in the keyhole. At the initial moment, t_0 (see Fig. 4(a)), the electron beam incident on the cold metal sample and electrons penetrate to some depth

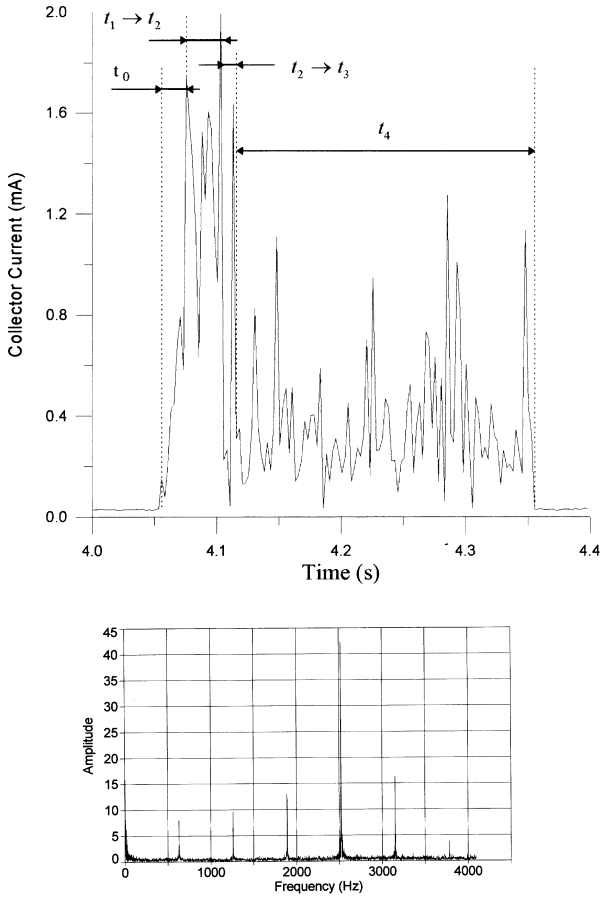

Figure 3. The collector signal during electron beam welding of carbon steel (a) and its Fourier spectra (b): $P = 3.6$ kW, $V = 0.5$ cm/s, $l_f = 512$ mA, $l = 60$ mA.

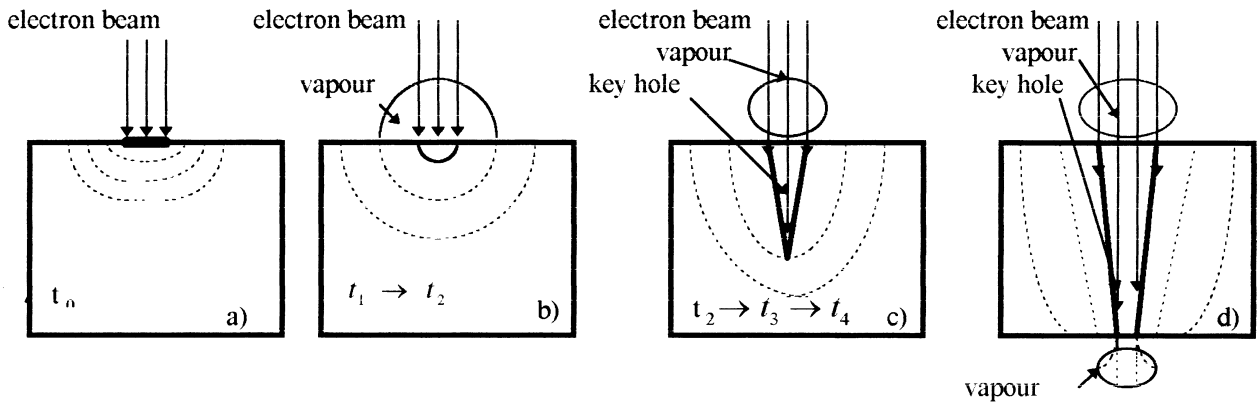

Figure 4. Schematic diagram of the electron beam welding process.

in the target. The kinetic energy of the electron penetrating is transformed into thermal energy and heating of the over surface layer begins. Evaporation starts when the surface temperature reaches a value dependent on the target material. This is represented by the time interval $t_1 - t_2$ in our case (Fig. 4(b)). The existence of a vapour phase results in fluctuations in the backscattered electron signal. These fluctuations are typical of the interaction of the accelerated electrons with a flat target and are a consequence of the scattering of the electron beam by metal vapours. There is scattering of the electrons on collision with the vapour atoms and subsequent focusing of the beam by compensation of the negative space charge in the electron beam by that are generated positive ions and the magnetic pinch of the beam,[15] as well as a gas focusing of the beam from the overcompensation of the beam negative charge at higher densities of metal and gas molecules in the keyhole.[16] The vapour pressure and temperature of rice leads to the keyhole formation $t_2 \rightarrow t_3 \rightarrow t_4$ (Fig. 4(c)). The level of the secondary emitted electron signal is reduced because of the electron beam incident on the front sides of the keyhole at an angle different of 90°. The metal evaporated from the front side of the keyhole, together with the portion of backscattered electrons, at reaching the rear side of the welding pool extract the local pressures on the back liquid metal walls of the plasma cavity. The signal preserves its nonstationary character t_4. Spectral analysis (Fig. 3(b)) shows that the frequency spectrum of the secondary electron emission signal is in the interval 0.5–4 kHz. The main reason for these instabilities is the interaction of the electron beam with metal vapour in the plasma cavity. The process of drilled cavity permits one to gain the depth of a few centimetres from the surface specimens within a few milliseconds.

The experimental results for when the light detector is above the target surface are shown in Fig. 5. A typical signal is observed from the photodiode in accordance with the temperature change in real-time on the surface point placed on 0.15 cm from directions of movement of the welded materials. Curve V1 is obtained when the linear energy of the electron beam is 3.2 kJ/cm. With an increase in the movement speed of the metal target curve V2 (decreasing the linear energy to 1.06 kJ/cm), both the width of the welding pool and the maximum temperature decreases. The results received for the light estimator placed under the target surface for dots placed at 0.1 mm from the welding seam axis are shown in Fig. 6. Curve 1 is obtained through a power of the

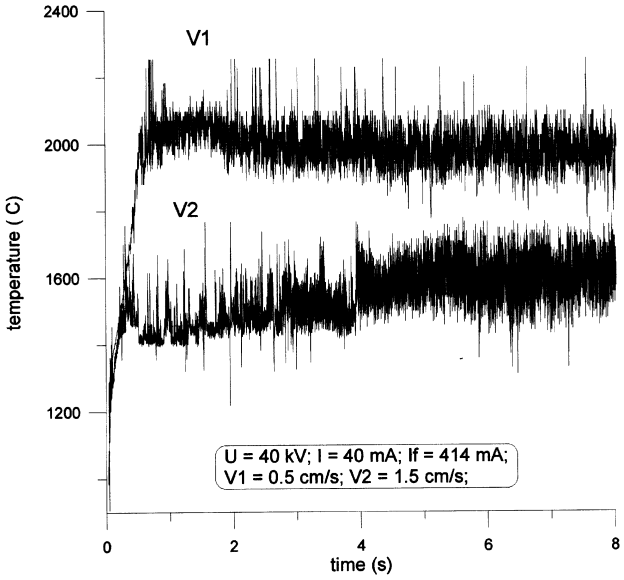

Figure 5. Evolution temperature on the surface of the welding pool.

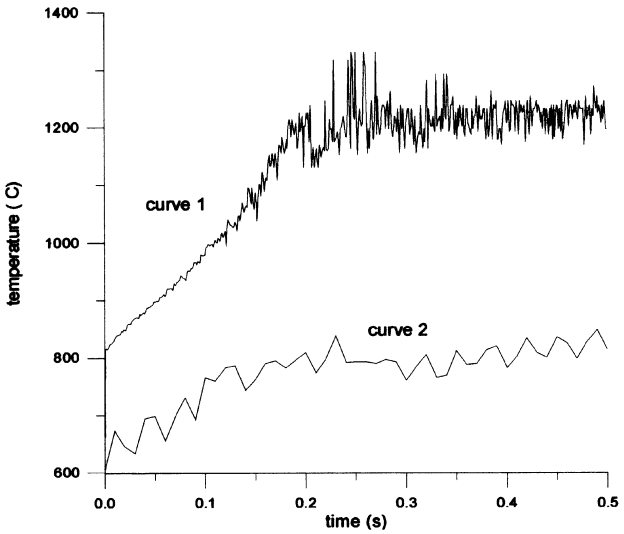

Figure 6. Evolution temperature on the reverse side of welding specimens.

electron beam equal to $P = 3$ kW and a welding speed equal to $V = 1$ cm/s. Curve 2 is obtained at the power of the electron beam equal to $P = 2.4$ kW while the welding speed and coordinates are the same. For curve 2, the welding pool's depth does not reach the thickness of the welded metal (closed keyhole mode at the bottom with an open keyhole at the surface; see Fig. 4(c)). When the power of the electron beam is increased in curve 1, the keyhole is opened at the target surface and back (Fig. 4(d)), and during this activity of electron beam forming a reverse seam and a crystallisation process of liquid drops occurs.

The weld pool images obtained with the CCD camera at constant electron beam power and different welding speeds are present in Fig. 7; this demonstrates that the effect of changing the electron beam welding parameters can be image monitoring.

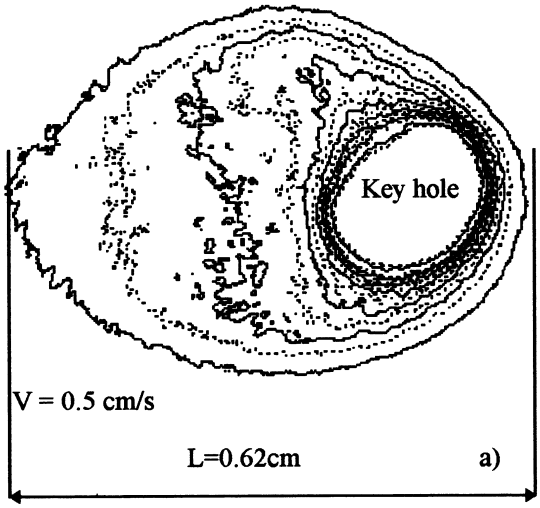

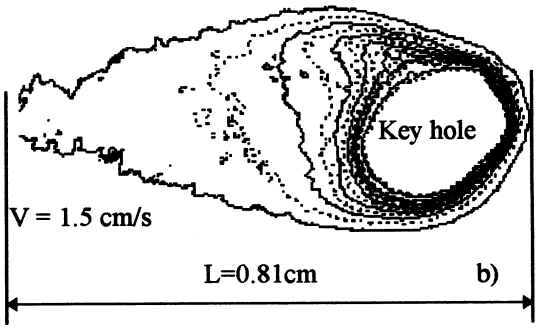

Figure 7. Weld pool image registered from a CCD camera: $P = 3.6$ kW, $I_f = 512$ mA, $I = 60$ mA.

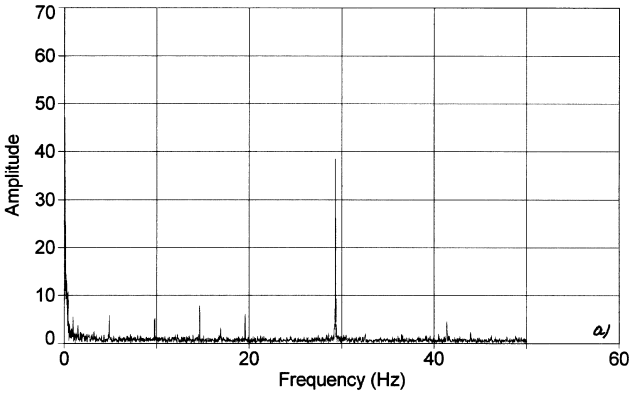

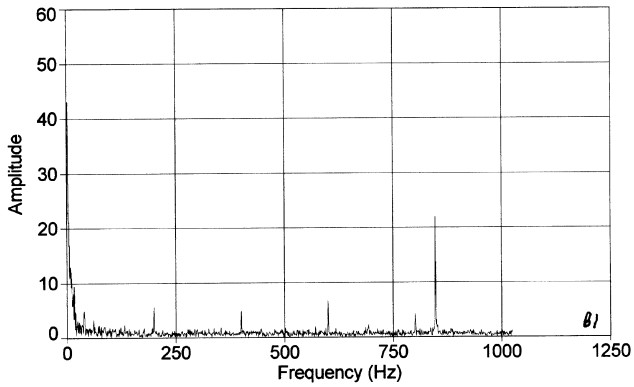

Figure 8. Fourier transform of a measured light from estimator process signals on the: (a) above welding pool; (b) reverse side of welding specimens.

With an increase of the welding speed the pool width decreased. The shapes of the welding pool and of the keyhole are apparently asymmetrical; the front side of the welding pool has a few layers of liquid metal compared with the back side of the pool. The dimensions of the cavity are more varying with time than the same characteristics of the welding pool.

Through a Fourier transformation of the signals from Figs 5 and 6, a typical amplitude–frequency relationship is formed as shown in Fig. 8. The Fourier transforms from the measured process signal from the photodiode under the welded specimen show pulsation frequencies for the welding seam root are at a low-frequency between 0.5–50 Hz (Fig. 8(a)). Results from Fig. 8(b) show that the spectral components of the temporal variation of the turbulent liquid fluxes in the melted zone on the surface of the welding pool are in the interval 5–850 Hz. The differences in the surface temperatures of the keyhole walls are resulting in differences of surface tension, which is responsible, together with the reactive pressure of evaporating atoms and hydrostatic forces, for the liquid metal movement and surface oscillations. The mass transport of the liquid metal from the melting front to the solidification phase boundary of the welding pool occurs around the plasma cavity walls through the side wall of the keyhole and in directions of the depth of the welding pool. It should also be noted that the mass transport of liquid metal in the welding pool influences largely the process of metal crystallisation, which in turn determines both the shape of the seam's cross-sections and

the presence of defects within its bulk. It has been previously shown in Ref. 17 that formation of such non-uniformity could be due to the generation of capillary waves in the welding pool. It is seen that the process transfers of the heated liquid metal are playing a major role in formation of the melted pool and keyhole during the electron beam welding. In addition, the processes of dissipation and focusing of an electron beam in evaporated metal must be taken into account too, because they influence directly the changes in the beam power density in the keyhole.

4. Conclusions

As a result of the carried out research work, it is obvious that the light-estimator on the basis of the photo diode and CCD camera has been possible to be used for high degree precision to follow the behaviour of the weld pool and keyhole during electron beam welding. The nature of the heat source is non-stationary and the dynamic processes taking place in both the welding pool and the plasma cavity play a dominant role in the formation of the welded seam during electron beam welding of metals. The main reasons for the non-stationary nature of the heat source are associated with the processes of dissipation of the electron beam in evaporated metal as well as with the intense mass transport of liquid metal in the welding pool. Experimentally are measured the periodical molten metal flows with low oscillation frequencies of the welding seam's root with frequency between 0.5–50 Hz and on the surface of the welding pool in the interval 5–850 Hz. The frequency spectrum of the secondary electron emission signal is in the interval 3–4 kHz as a result of interaction of the electron beam with evaporated metal in the plasma cavity.

Acknowledgement

This work was supported by the Bulgarian National Science Foundation (contract no. 540).

References

1. Rykalin, N., Uglov, A., Zuev, I. and Kokora, A., *Laser and Electron Beam Treatment of Materials*. Mashinostroeni, Moscow, 1985, p. 495.
2. Tong, H. and Gied, W., *Welding J*., 1970, **6,** 259.
3. Arata, Y., Matsuda, F. and Murakami, T., *Transaction of JWRI*, 1973, **2,** 23.
4. Weber, C., Funk, E. and McMaster, R., *Welding J*., 1972, **2,** 90.
5. Mara, G., Funk, E., McMaster, R. and Dence, P., *Welding J*., 1974, **6,** 53.
6. Tsukamoto, S. and Irie, H., *Transaction of JWRI*, 1993, **1,** 18.
7. Mitkevich, E. and Lokshin, ?., *Automatic Welding*, 1980, **9,** 26.
8. Petrov, P., Dyakov, T. and Mladenov, G., *Univ. Annual Report Technical Physics*, Sofia, 1987, **1,** 171.
9. Petrov, P., Georgiev, Ch. and Ivanov, R., *Int. J. for the Joining of Materials*, 1996, **4,** 152.
10. Eggers, H. and Ruge, J., *Schweissen und Schneiden*, 1971, **2,** 45.
11. Bashenko, V. and Mayer, R., *Automatic Welding*, 1976, **8,** 21.
12. Hiramoto, S., Ohmine, M. and Sakamoto, M., *Transaction of JWS*, 1992, **1,** 33.
13. Tenchov, Ch., Simeonova, D., Mitev, V. and Donkov, N., *Meas. Sci. Techno*., 1993, **4,** 1050.
14. Ohshima, K., Morita, M., Fujii, K., Yamamoto, M. and Kubota, T., *Transaction of JWS*, 1992, **1,** 17.
15. Gabovich, M., Kovalenko, V., Metallov, O. et al., *J. Technical Physics*, Moscow, 1977, **7,** 1569.
16. Ledovskoy, V. and Mladenov, G., *J. Technical Physics*, Moscow, 1970, **9,** 2260.
17. Stefanov, B., Petrov, P. and Pirgov, P., *Vacuum*, 1988, **11,** 1029.